Gaussian Markov Random Field Priors in Ionospheric 3-D Multi-Instrument Tomography

Johannes Norberg, Juha Vierinen, Lassi Roininen, Mikko Orispää, Kirsti Kauristie, William C. Rideout, Anthea J. Coster, and Markku S. Lehtinen

***Abstract*— In ionospheric tomography, the atmospheric electron density is reconstructed from different electron density related measurements, most often from ground-based measurements of satellite signals. Typically, ionospheric tomography suffers from two major complications. First, the information provided by measurements is insufficient and additional information is required to obtain a unique solution. Second, with necessary spatial and temporal resolutions, the problem becomes very high dimensional, and hence, computationally infeasible. With Bayesian framework, the required additional information can be given with prior probability distributions. The approach then provides physically quantifiable probabilistic interpretation for all model variables. Here, Gaussian Markov random fields (GMRFs) are used for constructing the prior electron density distribution. The use of GMRF introduces sparsity to the linear system, making the problem computationally feasible. The method is demonstrated over Fennoscandia with measurements from global navigation satellite system (GNSS) and low Earth orbit (LEO) satellite receiver networks, GNSS occultation receivers, LEO satellite Langmuir probes, and ionosonde and incoherent scatter radar measurements.**

***Index Terms*— Bayesian, Gaussian Markov random fields (GMRFs), ionospheric tomography, multi-instrument.**

I. Introduction

IONOSPHERIC tomography involves reconstruction of the atmospheric electron density within a volume, using a number of different measurements of electron density. The first studies on ionospheric tomography were made in [1]. A general introduction to the topic is provided in [2].

The electron density measurements can be divided to *indirect* and *direct* measurements. Indirect measurements refer here to satellite-to-ground and satellite-to-satellite measurements, where the measurements are modeled as integrals over electron density. In this paper, ground-based total electron content (TEC) measurements from global navigation satellite system (GNSS) and low Earth orbit (LEO) satellites and GNSS occultation TEC measurements are employed. These measurements have a lower accuracy of structural information, but typically a large spatial coverage can be attained. Direct measurements, such as different radar and satellite *in situ* measurements, provide relatively accurate structural information, but from a restricted area. This paper utilizes a satellite on-board Langmuir probe, incoherent scatter radars (ISRs), and ionosondes as direct measurements. However, even within these two categories the different measurements have different strengths and weaknesses, and are highly complementary. A 2-D simplification of measurement geometries is shown in Fig. 1.

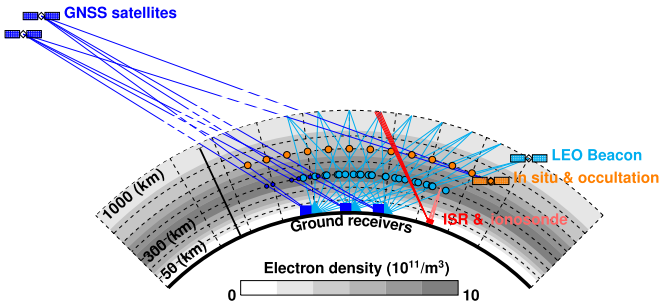

Fig. 1. Multi-instrument ionospheric electron density measurements. GNSS satellites provide line-integrated measurements all the way up to the plasmasphere, but as the satellites move relatively slow, the measurement geometry with respect to ground stations does not change significantly. The inclination angles of different GNSSs are low. LEO beacon satellites, which cover the ionosphere up to about 1000 km, can have a polar orbit and move relatively fast, allowing a 2-D slice of the ionosphere to be covered. LEO satellites with GNSS receivers provide variable look angles through the topside of the ionosphere. Langmuir probe provides the only *in situ* measurements available. Ionosondes provide localized bottomside profiles. ISRs provide localized profiles of electron density.

Typically, the available measurements are predominantly indirect satellite measurements with limited elevation angles, and the resulting information, particularly on vertical gradients is low. Consequently, the electron density cannot be solved uniquely without some additional structural information. The essential difference between different ionospheric tomography methods follows from how this information is implemented into the algorithm.

Manuscript received November 20, 2017; revised April 20, 2018; accepted May 23, 2018. Date of publication August 22, 2018; date of current version November 22, 2018. The work of J. Norberg was supported in part by the Academy of Finland under Grant 287679 and in part by the Regional Council of Lapland through European Regional Development Fund under Grant A70179. The work of L. Roininen was supported by the Academy of Finland under Project 307741 and Project 313709. The work of K. Kauristie was supported by the Academy of Finland under Grant 287679. *(Corresponding author: Johannes Norberg.)*

J. Norberg is with the Finnish Meteorological Institute, 00560 Helsinki, Finland, and also with Sodankylä Geophysical Observatory, University of Oulu, 99600 Sodankylä, Finland (e-mail: johannes.norberg@fmi.fi).

J. Vierinen is with the Department of Physics and Technology, University of Tromsø, 9019 Tromsø, Norway.

L. Roininen, M. Orispää, and M. S. Lehtinen are with Sodankylä Geophysical Observatory, University of Oulu, 90014 Oulu, Finland.

K. Kauristie is with the Finnish Meteorological Institute, 00560 Helsinki, Finland.

W. C. Rideout and A. J. Coster are with Haystack Observatory, Massachusetts Institute of Technology, Cambridge, MA 02139 USA.

Digital Object Identifier 10.1109/TGRS.2018.2847026

In [3], an extensive overview on different approaches and their development is provided. More recently, the topic has been studied in [4]–[7].

With Bayesian statistical approach, the required additional information can be given as a prior probability distribution. When Gaussian distributions are assumed, the prior information can be represented with the mean and covariance. In ionospheric tomography, the prior mean corresponds to most probable state of the atmospheric electron density, whereas the covariance describes its uncertainty. All the parameters included in the prior have, thus, a clear probabilistic interpretation with physical quantities. Hence, when the measurement and model errors are modeled correctly, in principle, the model has no free parameters that need to be calibrated. If additional tuning is nevertheless required, all the changes in the parameters have a clear meaning.

A comprehensive introduction to statistical inverse problems is provided in [8] and [9]. In ionospheric tomography, the Bayesian inference has been applied in [10]–[13]. The Ionospheric Data Assimilation Three-Dimensional (IDA3D) presented in [14] is based on the Three-Dimensional Variational Data Assimilation Technique (3DVAR) and uses slightly different terminology. However, with Gaussian prior and error distributions, the Bayesian statistical approach and 3DVAR are computationally identical.

The drawback of Bayesian approach is in computation, as the solution requires operations of large covariance matrices. In this paper, Gaussian Markov random field (GMRF) [15] priors for ionospheric tomography, presented in [12] and [13], are generalized to the 3-D multi-instrument case. The GMRF approach provides an extension to Bayesian and 3DVAR methods, as the prior covariance can be replaced with a sparse matrix approximation. Essentially, by implementing GMRF with sparse systems solvers, the computational cost in the high-dimensional matrix operations is reduced significantly.

This paper is organized as follows. In Section II, the models for different measurements are described. In Section III, the Bayesian statistical approach for linear tomography is revisited. In Section IV, the GMRF approximation of prior precision matrix is described, with a short summary of alternative ways to overcome the computational issues. In Section V, the performance of the considered method is presented. First, with a simulated example using the International Reference Ionosphere 2012 (IRI-2012) model as the unknown, and then with real multi-instrument data. The EISCAT ISR measurements are included for validation. Discussion and conclusion of the study are given in Sections VI and VII. The future plans are considered in Section VIII.

II. Measurements

The approach presented in this paper can exploit any measurement depending linearly on the ionospheric electron density with estimable measurement error. The electron density is given here as function $N_e(t, z)$, where t is the time and $z = \{z_{\text{lat}}, z_{\text{long}}, z_{\text{alt}}\} \in \mathbf{R}^3$ is the spatial coordinates.

A. Indirect Measurements

A GNSS TEC measurement along signal path $L_{sat,rec}(t)$ between satellite sat and receiver rec at time t can be modeled as a line integral

$$m_{sat,rec}(t) = \int_{L_{sat,rec}(t)} N_e(t, z)dl + a_{sat}(t) + b_{rec}(t) + \varepsilon_{sat,rec}(t) \tag{1}$$

where $a_{sat}(t)$ and $b_{rec}(t)$ are the receiver and satellite instrument biases. Discretization and assumption of time homogeneous ionosphere cause errors that need to be taken into account in the model. Here, the modeling errors are assumed independent of the unknown electron densities and added all together in $\varepsilon_{sat,rec}(t)$.

The forward model for GNSS occultation measurements is the same as for the ground-based measurements given in (1). The practical difference is that the on-board receiver is also in motion.

The relative TEC (RTEC) measurement between a LEO beacon satellite and a ground-based receiver can be modeled as

$$m_{sat,rec}(t) = \int_{L_{sat,rec}(t)} N_e(t, z)dl + \gamma_{sat,rec} + \varepsilon_{sat,rec}(t) \tag{2}$$

where the phase ambiguity is given with $\gamma_{sat,rec}$ and it is different for each signal lock [16].

Despite the similarity of the TEC measurement models, there are significant practical differences. By combining the different observables, the GNSS TEC does not suffer from the phase ambiguity [17]. The remaining GNSS satellite and receiver biases can have a significant effect on the TEC measurement. However, the changes in these biases are relatively slow and they can be estimated before the tomographic analysis [18], [19], thus the bias-corrected GNSS measurements can be assumed to be close to absolute TEC. On the other hand, as the bias estimation requires several simplifying assumptions, it is beneficial to keep the parameters a_{sat} and b_{rec} in the model and assume that after the bias correction, they are closer to zero, but not completely eliminated.

Due to lower signal frequencies (150 and 400 MHz), the LEO TEC measurements are more sensitive for detailed ionospheric structures, however, as the phase ambiguity is typically in the magnitude of current local maximum TEC, the measurement is relative and $\gamma_{sat,rec}$ needs to be solved as an additional unknown in the tomographic analysis. The orbital inclinations of GNSS satellites are relatively low [GPS 55°, Global Navigation Satellite System (GLONASS) 64.13°, GALILEO 56°]. For the polar regions, the low inclination induces low elevation angles making the measurements susceptible for larger errors. LEO beacon satellites can have orbital inclinations close to polar orbits (CASSIOPE/e-POP 80.99°, COSMOS 2407 and 2463 83°), thus providing high-elevation measurements also from high-latitude receivers. Following from the higher orbital altitudes of GNSS satellites (GLONASS 19 140 km, GPS 20 180 km, and GALILEO 23 222 km), the plasmaspheric contribution in the TEC measurement can be significant. With orbital altitudes around 1000 km, there is no plasmaspheric contribution in the LEO

RTEC measurements. The lower altitude also results in a higher relative satellite velocity, and hence better spatial coverage for the individual satellite when present. Multiple GNSS satellites can be viewed from all locations and at all times, especially now there are several satellite constellations. GNSS observations are also easily obtained as large receiver networks exist. This differs from the case of LEO satellites as there are fewer receivers (LEO receivers are built specifically for this purpose) and there are only few suitable satellites. Hence, in general, the GNSS TEC measurements are the most important data component, providing constant spatiotemporal coverage with absolute measurements. LEO RTEC measurements provide more detailed information and provide higher elevation data in polar areas, but the spatiotemporal availability is inferior to GNSS.

B. Direct Measurements

When the electron density is detected in a specific location, as is the case with different radar and satellite *in situ* measurements, the direct measurement from instrument $\mathcal{I}$ can be modeled simply as

$$m_{\mathcal{I}}(t,z) = N_{\mathrm{e}}(t,z) + \varepsilon_{\mathcal{I}}(t,z). \tag{3}$$

With satellite *in situ* measurements $z = (z_{\mathrm{lat}}, z_{\mathrm{lon}}, z_{\mathrm{alt}})$ is the location of the Langmuir probe, and with ISR, it is the location of measurement integration. With inverted, real-height ionosonde electron density profiles $(z_{\mathrm{lat}}, z_{\mathrm{long}})$ is the location of the instrument and z_{alt} is the real reflection height.

In comparison to any indirect measurement, these measurements provide significantly more accurate and detailed information on ionospheric structures. As a downside, the spatial coverage of measurements is typically limited.

III. Bayesian Statistical Approach

By assuming stationary electron density for a given time interval and discretizing the measurement models (1)–(3), all the ionospheric measurements can be combined and written as

$$\mathbf{m} = \mathbf{A}\mathbf{X} + \boldsymbol{\varepsilon} \tag{4}$$

where $\mathbf{m} \in \mathbf{R}^M$ is a vector of all measurements. Geometry matrix $\mathbf{A} \in \mathbf{R}^{M\times N}$ is a linear mapping from discretized spatial domain to measurement space. Vector

$$\mathbf{X} = \begin{pmatrix} \mathbf{x} \\ \boldsymbol{\theta} \end{pmatrix} \in \mathbf{R}^N$$

consists of unknown electron densities $\mathbf{x} \in \mathbf{R}^n$, as well as all the additional unknown error parameters $\boldsymbol{\theta} = (a_{\mathrm{sat}_1} \ldots a_{\mathrm{sat}_A}, b_{\mathrm{rec}_1}, \ldots, b_{\mathrm{rec}_B}, \gamma_{1,1} \ldots \gamma_{C,D}, \rho)^{\mathrm{T}}$, where ρ is the plasmaspheric electron density contribution per meter, A, B, C, and D are the counts of GNSS satellites, GNSS receivers, LEO satellites, and LEO receivers, respectively, and $n + A + B + C \times D + 1 = N$. Vector $\boldsymbol{\varepsilon} \in \mathbf{R}^M$ contains all the measurement and modeling errors. Here, it is assumed that the error vector follows a multivariate normal distribution

$$\boldsymbol{\varepsilon} \sim \mathcal{N}(\mathbf{0}, \boldsymbol{\Sigma}_{\varepsilon})$$

and that the realistic states of the ionosphere and additional parameters can be described satisfactorily with a prior distribution, which is also multivariate normal

$$\mathbf{X} \sim \mathcal{N}(\mathbf{X}_{\mathrm{pr}}, \boldsymbol{\Sigma}_{\mathrm{pr}}) \tag{5}$$

where $\mathbf{X}_{\mathrm{pr}}$ is the prior mean of the ionosphere and additional parameters. Covariance $\boldsymbol{\Sigma}_{\mathrm{pr}}$ describes the related prior uncertainties. Following the Bayes theorem [9], the posterior distribution for $\mathbf{X}$ is then also a multivariate normal distribution

$$\mathbf{X}|\mathbf{m} \sim \mathcal{N}(\mathbf{X}_{\mathrm{MAP}}, \boldsymbol{\Sigma}_{\mathrm{post}})$$

where *maximum a posteriori* (MAP) estimator

$$\mathbf{X}_{\mathrm{MAP}} = \boldsymbol{\Sigma}_{\mathrm{post}}\left(\mathbf{A}^{\mathrm{T}}\boldsymbol{\Sigma}_{\varepsilon}^{-1}\mathbf{m} + \boldsymbol{\Sigma}_{\mathrm{pr}}^{-1}\mathbf{X}_{\mathrm{pr}}\right) \tag{6}$$

and posterior covariance estimator

$$\boldsymbol{\Sigma}_{\mathrm{post}} = \left(\mathbf{A}^{\mathrm{T}}\boldsymbol{\Sigma}_{\varepsilon}^{-1}\mathbf{A} + \boldsymbol{\Sigma}_{\mathrm{pr}}^{-1}\right)^{-1}. \tag{7}$$

In an application to ionospheric tomography, the MAP estimator $\mathbf{X}_{\mathrm{MAP}}$ can be understood as the most probable state of the ionospheric electron density and other unknown parameters, whereas the remaining uncertainty is given with the error covariance $\boldsymbol{\Sigma}_{\mathrm{post}}$.

IV. Computation

The downside of Bayesian statistical approach for inverse problems is that the assumption of a proper prior distribution (5) results with a dense $N \times N$ covariance matrix $\boldsymbol{\Sigma}_{\mathrm{pr}}$. The estimators (6) and (7) contain inverted covariance matrices and the posterior covariance estimator involves one more matrix inversion. Hence, the solution becomes exceedingly demanding computationally. To ease the computational burden, the dimensions would need to be reduced or sparsity would need to be introduced into the linear system. Two previously applied approaches are first revisited, before introducing the GMRF approach for sparse approximation of the covariance matrix.

A. Generalized Tikhonov Regularization

When independent measurement errors are assumed, the measurement covariance matrix is diagonal, $\boldsymbol{\Sigma}_{\varepsilon} = \sigma_{\varepsilon}^2\mathbf{I}$, and due to the nature of the measurements, the geometry matrix $\mathbf{A}$ is a sparse matrix. If the inverted covariance matrix, i.e., the prior precision matrix $\boldsymbol{\Sigma}_{\mathrm{pr}}^{-1}$ could be given also as a sparse matrix, the memory required for storage would decrease and optimized solvers for sparse linear systems could be utilized for the computation.

In more general sense, the MAP estimator (6) is a regularized least squares solution. Selecting $\boldsymbol{\Sigma}_{\mathrm{pr}}^{-1} = 0$ reduces it to ordinary least squares estimator. With $\boldsymbol{\Sigma}_{\mathrm{pr}}^{-1} = \delta\mathbf{I}$, the estimator corresponds to Ridge regression and Tikhonov regularized solution. When $\boldsymbol{\Sigma}_{\mathrm{pr}}^{-1}$ is any suitably chosen matrix, the estimator is called the generalized Tikhonov regularization [9]. Typically, $\boldsymbol{\Sigma}_{\mathrm{pr}}^{-1} = \delta\boldsymbol{\Gamma}^{\mathrm{T}}\boldsymbol{\Gamma}$, where $\boldsymbol{\Gamma}$ is a difference matrix. These can be extremely sparse systems and the inversion in (7) is possible even for relatively high-dimensional problems. With these approaches, it is possible to add structural constraints for

the solution. For ionospheric tomography, in [4] and [10], a vertical weight profile is included in matrices $\mathbf{\Gamma}$ to regularize the problem more strictly at the very low and high altitudes and to allow more variability to electron densities at altitudes where the highest values and dynamics are expected. The constraint ends up to provide essentially similar information than a full prior covariance would, but as it lacks some of the interpretation, it requires *ad hoc* calibration.

B. Data Space Solution

With matrix inversion lemma, the MAP estimator (6) can be written equivalently as

$$\mathbf{X}_{\mathrm{MAP}} = \mathbf{X}_{\mathrm{pr}} + \mathbf{\Sigma}_{\mathrm{pr}}\mathbf{A}^{\mathrm{T}}\left(\mathbf{A}\mathbf{\Sigma}_{\mathrm{pr}}\mathbf{A}^{\mathrm{T}} + \mathbf{\Sigma}_{\varepsilon}\right)^{-1}(\mathbf{m} - \mathbf{A}\mathbf{X}_{\mathrm{pr}}) \quad (8)$$

and

$$\mathbf{\Sigma}_{\mathrm{post}} = \mathbf{\Sigma}_{\mathrm{pr}} - \mathbf{\Sigma}_{\mathrm{pr}}\mathbf{A}^{\mathrm{T}}\left(\mathbf{A}\mathbf{\Sigma}_{\mathrm{pr}}\mathbf{A}^{\mathrm{T}} + \mathbf{\Sigma}_{\varepsilon}\right)^{-1}\mathbf{A}\mathbf{\Sigma}_{\mathrm{pr}}. \quad (9)$$

This form is preferred by IDA3D [14] and in the standard formulation of Kalman filter. The advantage is that the inversion is done for $M \times M$ matrix, whereas in (6), an $N \times N$ matrix is inverted. Typically, in ionospheric tomography, $M \ll N$ which can unburden the inversion. Here, the computational bottleneck is in representing and storing the covariance matrix $\mathbf{\Sigma}_{\mathrm{pr}}$ and performing the matrix multiplications. In case of global ionospheric tomography, it can be assumed that locations with long enough distance have a zero correlation. This covariance tapering [20] introduces sparsity to the system. However, in local tomography, the correlation lengths extend over the domain, hence, the prior covariance is a dense matrix.

C. Gaussian Markov Random Field Prior

The idea here is the following. As the estimator (6) does not require actual covariance matrices, but rather precision matrices, a sparse precision matrix $\mathbf{Q}$ is constructed so that

$$\mathbf{Q}^{-1} \approx \mathbf{\Sigma}_{\mathrm{pr}} \quad (10)$$

where the matrix $\mathbf{Q}$ is built with the formalism of GMRFs. When parameterized correctly, a GMRF gives rise to a known spatial covariance. So, even though the actual covariance matrix is never constructed, the precision matrix can be determined by its covariance properties.

The detailed theoretical background for these types of GMRFs is given in [21]–[24]. Here, an example is given, where the target precision $\mathbf{\Sigma}_{\mathrm{pr}}^{-1}$ is determined with a squared exponential covariance function

$$\mathrm{Cov}(z_i - z_j) = \alpha(z_i, z_j)\exp\left[-\frac{1}{2}\left(\left(\frac{z_{i,\mathrm{lat}} - z_{j,\mathrm{lat}}}{\ell_{\mathrm{lat}}}\right)^2 + \left(\frac{z_{i,\mathrm{long}} - z_{j,\mathrm{long}}}{\ell_{\mathrm{long}}}\right)^2 + \left(\frac{z_{i,\mathrm{alt}} - z_{j,\mathrm{alt}}}{\ell_{\mathrm{alt}}}\right)^2\right)\right] \quad (11)$$

where $\ell_{\mathrm{lat}}, \ell_{\mathrm{long}}$, and $\ell_{\mathrm{alt}} > 0$ are the correlation lengths homogeneous in each coordinate direction and $\alpha(z_i, z_j) > 0$ is a location-dependent variance mask.

Following [24], an anisotropic continuous GMRF with a covariance approximating (11) can be formed as a solution to a stochastic partial differential equation

$$\begin{pmatrix} \sqrt{c_0}I \\ \sqrt{c_1}\ell_{\mathrm{lat}}\partial_{\mathrm{lat}} \\ \sqrt{c_1}\ell_{\mathrm{alt}}\partial_{\mathrm{alt}} \\ \sqrt{c_1}\ell_{\mathrm{long}}\partial_{\mathrm{long}} \\ \sqrt{c_2}\left(\ell_{\mathrm{lat}}^2\partial_{\mathrm{lat}}^2 + \ell_{\mathrm{alt}}^2\partial_{\mathrm{alt}}^2 + \ell_{\mathrm{long}}^2\partial_{\mathrm{long}}^2\right) \end{pmatrix} X(z) = \sqrt{\alpha(z)\ell_{\mathrm{lat}}\ell_{\mathrm{alt}}\ell_{\mathrm{long}}} \begin{pmatrix} \mathcal{W}^{(0)}(z) \\ \mathcal{W}^{(1,\mathrm{lat})}(z) \\ \mathcal{W}^{(1,\mathrm{alt})}(z) \\ \mathcal{W}^{(1,\mathrm{long})}(z) \\ \mathcal{W}^{(2)}(z) \end{pmatrix} \quad (12)$$

where $X(z)$ and $\mathcal{W}^{(\cdot)}(z)$, $z \in \mathbf{R}^3$ are the continuous random fields and independent continuous white noise fields, respectively. For squared exponential covariance function (11), the shape parameters $c_k = 2^{-k}/k!$, with k corresponding to the order of the derivative.

To make (12) applicable for computations, there are two objects to discretize the differential operator on the left-hand side and the white noise on the right-hand side. By using finite difference methods, a 3-D domain is defined with dimensions $n_{\mathrm{lat}} \times n_{\mathrm{alt}} \times n_{\mathrm{long}} = n$ and voxel widths h_{lat}, h_{alt} and h_{long} in the different coordinate directions. To simplify the following formulation, new parameters $s_{\mathrm{lat}} := (h_{\mathrm{lat}}/\ell_{\mathrm{lat}})$, $s_{\mathrm{alt}} := (h_{\mathrm{alt}}/\ell_{\mathrm{alt}})$ and $s_{\mathrm{long}} := (h_{\mathrm{long}}/\ell_{\mathrm{long}})$ are defined. Here, only the unknown electron densities $\mathbf{x} = (x_1, \ldots, x_j, \ldots x_n)^{\mathrm{T}}$ are considered. The additional error parameters $\boldsymbol{\theta}$ are independent of $\mathbf{x}$ and are included after the field is discretized at the end of the section.

The discrete approximation for white noise is

$$W_j^{(k)} \sim \mathcal{N}\left(0, \frac{\alpha_j}{c_k}\frac{1}{s_{\mathrm{lat}}s_{\mathrm{alt}}s_{\mathrm{long}}}\right)$$

where the superscript k is an index for the order of difference. The discrete white noise process is then set as

$$x_j = W_j^{(0)}. \quad (13)$$

The first-order differences are

$$\begin{aligned} \Delta_{\mathrm{lat}}x_j &:= \frac{1}{s_{\mathrm{lat}}}(x_{j+1} - x_j) = W_j^{(1,\mathrm{lat})} \\ \Delta_{\mathrm{alt}}x_j &:= \frac{1}{s_{\mathrm{alt}}}(x_{j+n_{\mathrm{lat}}} - x_j) = W_j^{(1,\mathrm{alt})} \\ \Delta_{\mathrm{long}}x_j &:= \frac{1}{s_{\mathrm{long}}}(x_{j+n_{\mathrm{lat}}n_{\mathrm{alt}}} - x_j) = W_j^{(1,\mathrm{long})} \end{aligned} \quad (14)$$

where the first superscript on the right-hand side is the order of difference and the second superscript is the effective coordinate direction. The second-order differences are given as

$$\Delta^2 x_j := \Delta_{\mathrm{lat}}^2 x_j + \Delta_{\mathrm{alt}}^2 x_j + \Delta_{\mathrm{long}}^2 x_j = W_j^{(2)} \quad (15)$$

where

$$\Delta^2_{\text{lat}} x_j := \left(\frac{x_{j+1} - x_j}{s_{\text{lat}}} - \frac{x_j - x_{j-1}}{s_{\text{lat}}} \right) \frac{1}{s_{\text{lat}}}$$
$$\Delta^2_{\text{alt}} x_j := \left(\frac{x_{j+n_{\text{lat}}} - x_j}{s_{\text{alt}}} - \frac{x_j - x_{j-n_{\text{lat}}}}{s_{\text{alt}}} \right) \frac{1}{s_{\text{alt}}}$$
$$\Delta^2_{\text{long}} x_j := \left(\frac{x_{j+n_{\text{lat}}n_{\text{alt}}} - x_j}{s_{\text{long}}} - \frac{x_j - x_{j-n_{\text{lat}}n_{\text{alt}}}}{s_{\text{long}}} \right) \frac{1}{s_{\text{long}}}.$$

The white noise $W_j^{(k)}$ can be standardized as

$$\sqrt{\frac{c_k}{\alpha_j} s_{\text{lat}} s_{\text{alt}} s_{\text{long}}}\ W_j^{(k)} = \xi_j^{(k)} \sim \mathcal{N}(0,1)$$

and for all indices j and k as

$$\boldsymbol{\xi_0} = \left(\xi_1^{(0)}, \ldots, \xi_n^{(0)}\right) \sim \mathcal{N}(\mathbf{0}, \mathbf{I}_n),$$
$$\boldsymbol{\xi_1} = \left(\xi_1^{(1,\text{lat})}, \ldots, \xi_n^{(1,\text{long})}\right) \sim \mathcal{N}(\mathbf{0}, \mathbf{I}_{3n}),$$
$$\boldsymbol{\xi_2} = \left(\xi_1^{(2)}, \ldots, \xi_n^{(2)}\right) \sim \mathcal{N}(\mathbf{0}, \mathbf{I}_n).$$

Now the differences (13)–(15) can be written in matrix form as follows.

For the standardized white noise process, the matrix form is

$$\sqrt{\frac{c_0}{\boldsymbol{\alpha}} s_{\text{lat}} s_{\text{alt}} s_{\text{long}}} \circ [\mathbf{I}_{n_{\text{long}}} \otimes \mathbf{I}_{n_{\text{alt}}} \otimes \mathbf{I}_{n_{\text{lat}}}]\mathbf{x} =: \mathbf{L_0 x} = \boldsymbol{\xi_0} \quad (16)$$

where $\mathbf{I}$s are identity matrices with diagonal length corresponding to the subscript, the variance mask is given as

$$\frac{1}{\boldsymbol{\alpha}} := \begin{bmatrix} 1 \\ \vdots \\ 1 \end{bmatrix} \otimes \left[\frac{1}{\alpha_1}, \ldots, \frac{1}{\alpha_n} \right] \in \mathbf{R}^{n \times n}$$

the symbol "$\circ$" is the Hadamard product and the symbol "$\otimes$" is the Kronecker product.

For the first-order differences, the different coordinate directions are given in matrix form separately at their own rows

$$\begin{pmatrix} \sqrt{\frac{c_1}{\boldsymbol{\alpha}} \frac{s_{\text{alt}} s_{\text{long}}}{s_{\text{lat}}}} \circ [\mathbf{I}_{n_{\text{long}}} \otimes \mathbf{I}_{n_{\text{alt}}} \otimes \mathbf{L}_{n_{\text{lat}}}] \\ \sqrt{\frac{c_1}{\boldsymbol{\alpha}} \frac{s_{\text{lat}} s_{\text{long}}}{s_{\text{alt}}}} \circ [\mathbf{I}_{n_{\text{long}}} \otimes \mathbf{L}_{n_{\text{alt}}} \otimes \mathbf{I}_{n_{\text{lat}}}] \\ \sqrt{\frac{c_1}{\boldsymbol{\alpha}} \frac{s_{\text{lat}} s_{\text{alt}}}{s_{\text{long}}}} \circ [\mathbf{L}_{n_{\text{long}}} \otimes \mathbf{I}_{n_{\text{alt}}} \otimes \mathbf{I}_{n_{\text{lat}}}] \end{pmatrix} \mathbf{x} =: \mathbf{L_1 x} = \boldsymbol{\xi_1} \quad (17)$$

where $\mathbf{L}_{n_{\text{lat}}}$, $\mathbf{L}_{n_{\text{alt}}}$, and $\mathbf{L}_{n_{\text{long}}}$ are difference matrices with structure

$$\begin{pmatrix} -1 & 1 & & \\ & -1 & 1 & \\ & & \ddots & \ddots \\ 1 & & & -1 \end{pmatrix}$$

and dimensions $n_{\text{lat}} \times n_{\text{lat}}$, $n_{\text{alt}} \times n_{\text{alt}}$, and $n_{\text{long}} \times n_{\text{long}}$, correspondingly.

The second-order differences are given in matrix form as

$$\left(\sqrt{\frac{c_2}{\boldsymbol{\alpha}} \frac{s_{\text{alt}} s_{\text{long}}}{s_{\text{lat}}^3}} \circ \left[\mathbf{I}_{n_{\text{long}}} \otimes \mathbf{I}_{n_{\text{alt}}} \otimes \left(\mathbf{L}_{n_{\text{lat}}}^{\text{T}} \mathbf{L}_{n_{\text{lat}}} \right) \right] \right.$$
$$+ \sqrt{\frac{c_2}{\boldsymbol{\alpha}} \frac{s_{\text{lat}} s_{\text{long}}}{s_{\text{alt}}^3}} \circ \left[\mathbf{I}_{n_{\text{long}}} \otimes \left(\mathbf{L}_{n_{\text{alt}}}^{\text{T}} \mathbf{L}_{n_{\text{alt}}} \right) \otimes \mathbf{I}_{n_{\text{lat}}} \right]$$
$$\left. + \sqrt{\frac{c_2}{\boldsymbol{\alpha}} \frac{s_{\text{lat}} s_{\text{alt}}}{s_{\text{long}}^3}} \circ \left[\left(\mathbf{L}_{n_{\text{long}}}^{\text{T}} \mathbf{L}_{n_{\text{long}}} \right) \otimes \mathbf{I}_{n_{\text{alt}}} \otimes \mathbf{I}_{n_{\text{lat}}} \right] \right) \mathbf{x} =: \mathbf{L_2 x} = \boldsymbol{\xi_2}. \quad (18)$$

Finally, the matrix equations (16)–(18) can be stacked as

$$\begin{pmatrix} \mathbf{L_0} \\ \mathbf{L_1} \\ \mathbf{L_2} \end{pmatrix} \mathbf{x} = \begin{pmatrix} \boldsymbol{\xi_0} \\ \boldsymbol{\xi_1} \\ \boldsymbol{\xi_2} \end{pmatrix} =: \mathbf{L x} = \boldsymbol{\xi} \sim \mathcal{N}(\mathbf{0}, \mathbf{I}_{5n}). \quad (19)$$

The solution for $\mathbf{x}$ is the desired prior GMRF with an $n \times n$ precision matrix $\mathbf{L}^{\text{T}}\mathbf{L}$. The precision matrix can then be completed to $N \times N$ dimensions, to also take into account the additional error parameters $\boldsymbol{\theta}$ as

$$\begin{pmatrix} \mathbf{L}^{\text{T}}\mathbf{L} & 0 \\ 0 & \text{diag}\left(\boldsymbol{\sigma}_{\boldsymbol{\theta}_{\text{pr}}}^{-2}\right) \end{pmatrix} = \mathbf{Q} \quad (20)$$

where a prior distribution $\boldsymbol{\theta} \sim \mathcal{N}\left(\boldsymbol{\theta}_{\text{pr}}, \text{diag}\left(\boldsymbol{\sigma}^2_{\boldsymbol{\theta}_{\text{pr}}}\right)\right)$ is assumed, with prior mean $\boldsymbol{\theta}_{\text{pr}} \in \mathbf{R}^{(N-n)}$ and diagonal prior covariance matrix $\text{diag}\left(\boldsymbol{\sigma}^2_{\boldsymbol{\theta}_{\text{pr}}}\right) \in \mathbf{R}^{(N-n)\times(N-n)}$.

Now, the matrix inversion $\mathbf{Q}^{-1}$ is a close approximation for $\boldsymbol{\Sigma}_{\text{pr}}$, with the covariance structure for $\mathbf{x}$ given in (11). Most importantly, the matrix $\mathbf{L}^{\text{T}}\mathbf{L}$ in $\mathbf{Q}$ consists only of $25 \times n$ nonzero elements, whereas the corresponding covariance would be a dense $n \times n$ matrix. Obviously, in 3-D cases, n is orders of magnitude greater than 25.

With the given discretization, the methodology provides inhomogeneous GMRF priors, which take into account the discretization of the unknown, hence providing a discretization-invariant reconstruction method (for references on discretization invariance, see [22]). From the practical point of view, this means that the posterior distributions and reconstructions on different computational meshes are essentially the same, given dense enough mesh. In this section, in (13)–(19), a regular discretization was used. However, an irregular grid could be used as well, and in the example of Section V, this is the case. The use of irregular discretization is straightforward, but, as the parameters h and s become vectors and for one index, the discretization step can be different depending on which side the difference is taken, the indexing of the previous equations would become more difficult to follow.

V. Results

A time window on November 8, 2015 from 10:18:00 to 10:38:00 UTC is chosen for analysis as all the observation types described in Section II are available at that time. The corresponding magnetic local time interval at EISCAT site, Tromsø, is approximately from 12:35 to 12:55.

The analyzed period was geomagnetically quiet with the Auroral Electrojet index [25] being clearly below 100 nT. However, a major geomagnetic storm took place during the previous day and during the prior 12 h, a couple of minor (B and C-level) solar flares were apparent. During the afternoon and evening hours of November 8, auroral electrojet activity index activity enhanced again to levels above 1000 nT.

The receiver and measurement locations are presented in Figs. 2 and 3. The observations include: 1) seven in-sight GPS satellites measured with 81 Geotrim,[1] 324 SWEPOS,[2] and 123 International GNSS Service receivers, all first collected with 30 s and then averaged to 300 s time resolution; 2) simultaneous COSMOS 2407 and 2463 LEO beacon

[1] http://www.geotrim.fi

[2] https://swepos.lantmateriet.se

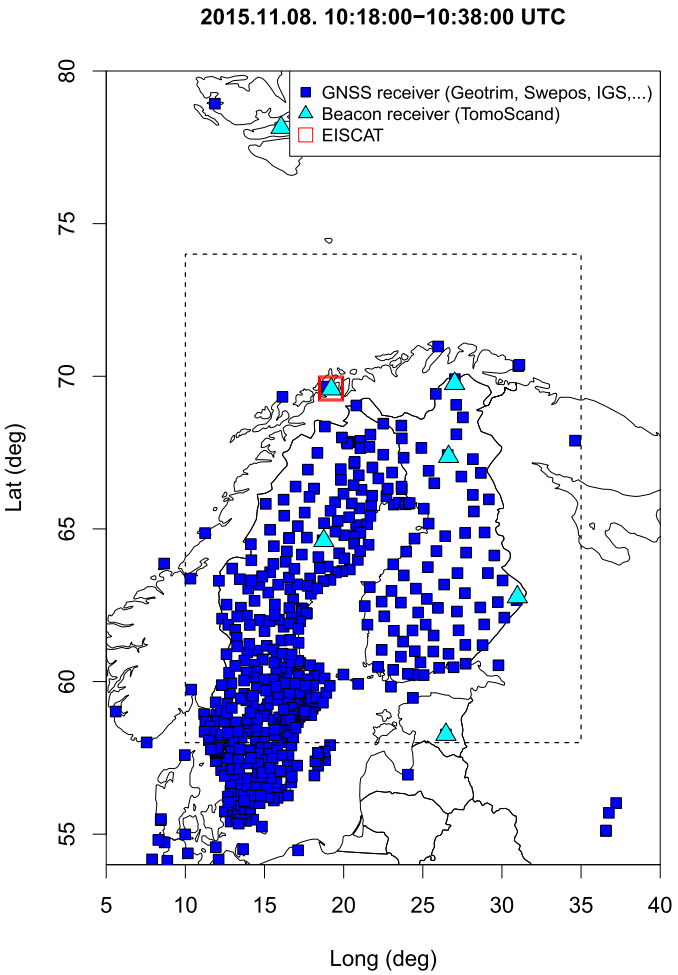

Fig. 2. Locations of available ground-based instruments. Only the area of the dashed rectangle is shown in the following 3-D reconstructions.

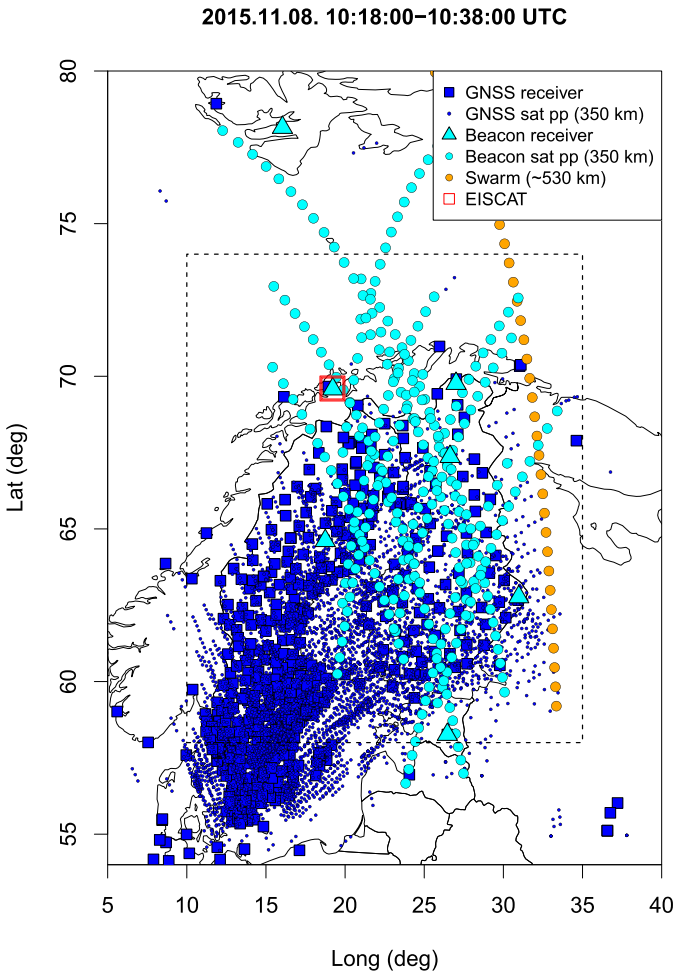

Fig. 3. Locations of available ground-based instruments, ionospheric pierce points of satellite measurements, and Swarm satellite measurements. Only the area of the dashed rectangle is shown in the following 3-D reconstructions.

satellite overflights, both measured with seven ground-based TomoScand receivers [16]; 3) Swarm B satellite overflight providing Langmuir probe *in situ* measurements, as well as satellite occultation TEC measurements from one GPS satellite [26]; 4) EISCAT Dynasonde electron density profiles with 120 s time resolution [3] [27]; 5) EISCAT ultra high frequency (UHF) ISR measurements with elevation $= 35°$ and azimuth $= 145°$; and 6) EISCAT very high frequency (VHF) ISR measurements with elevation $= 90°$.[4]

Two prior mean options were used. First, a simple zero profile and then an altitude dependent ionosonde profile. With the ionosonde prior mean, the lower profile is taken as the altitude medians from 10 EISCAT Dynasonde profiles from the given time interval. Above the peak electron density altitude, an exponential profile is used with scale height of 180 km. For covariance, a squared exponential spatial function was chosen with correlation lengths: $\ell_{\text{lat}} = 20°, \ell_{\text{long}} = 25°$, and $\ell_{\text{alt}} = 400$ km. The correlation length is defined here as the distance where the covariance drops to 10% of variance. The altitude-dependent variance scaling profile $\boldsymbol{\alpha}$ is determined here with standard deviation (SD). The SD is given as a Chapman profile with peak altitude taken from EISCAT Dynasonde real-height peak and electron density corresponds to 50% of Dynasonde's peak electron density. The scale height is set to 140 km.

Approximations for the measurement error SDs are provided with the data. SD of 2 total electron content units (TECU) is assumed for modeling errors. For preprocessed GPS station biases, zero mean with 1 TECU SD and for GPS satellite biases zero mean with 0.1 TECU SD is assumed. The phase constants of LEO measurements are given an SD of 10 TECU. The plasmaspheric contribution above 1250 km altitude is assumed to be uniformly 0.1 TECU for 2×10^4 km with SD of 0.1 TECU.

The 3-D spatial domain chosen for analysis covers latitudes from 54° to 80°, with 2° resolution at boundaries and 0.25° resolution between the latitudes 58° and 74°; longitudes from 5° to 40° with 2° resolution at boundaries and 0.25° resolution between the longitudes 9° and 36°; and altitudes from ground level to 750 km with 25 km resolution and then up to 1250 km with 50 km resolution. This results as a grid of $n = 309\,120$ voxels. Combined with phase constant, bias, and plasma parameters, the total number of unknown variables in this case is $N = 309\,648$.

Now, when using the GMRF approach of Section IV, the resulting prior precision matrix has only 0.008% nonzero

[3] http://dynserv.eiscat.uit.no/DD/login.php
[4] https://www.eiscat.se/madrigal/

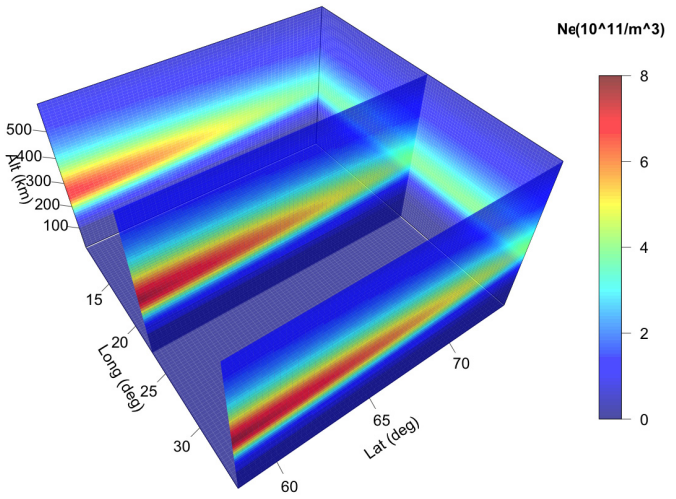

Fig. 4. IRI-2012 model electron density with default parameters for November 8, 2015 10:30:00 UTC.

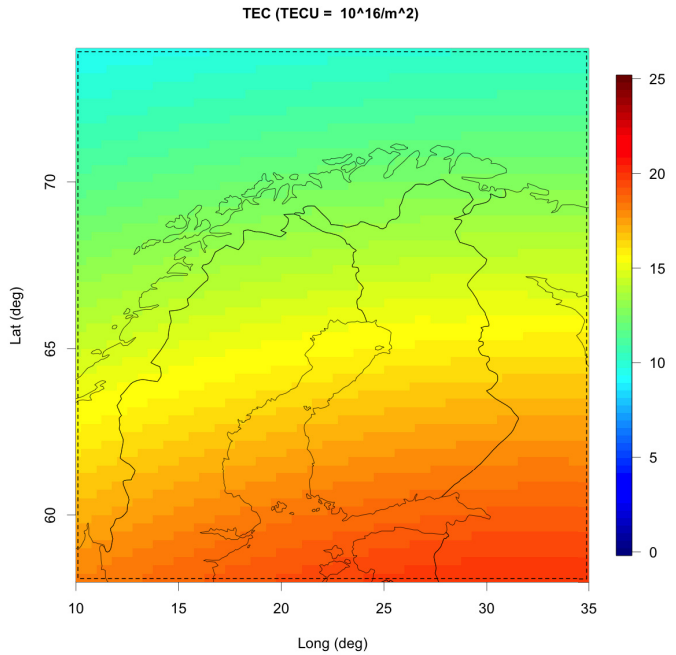

Fig. 5. Vertically integrated TEC (0–1250 km) from IRI-2012 model electron density with default parameters for November 8, 2015 10:30:00 UTC.

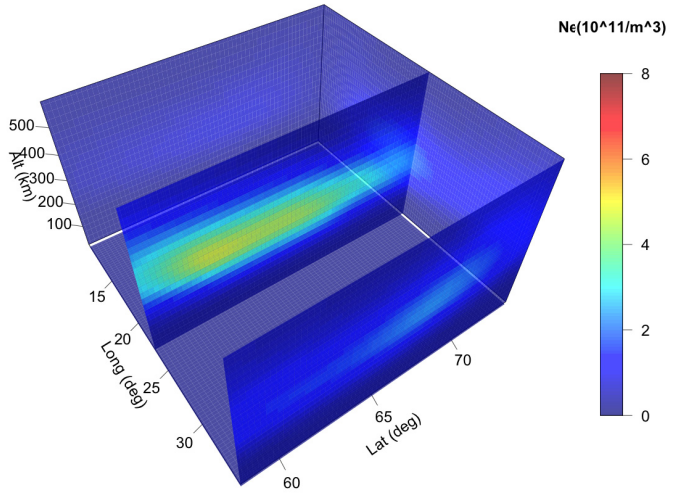

Fig. 6. Simulation case: reconstruction from simulated LEO beacon measurements with zero-mean GMRF prior.

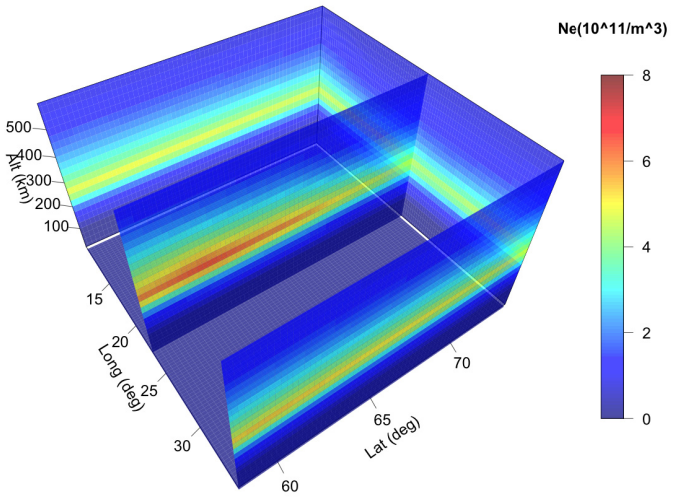

Fig. 7. Simulation case: reconstruction from simulated ground-based LEO satellite measurements. Simulated ionosonde measurements are used in the scaling of GMRF prior mean and variance mask.

elements. When the prior precision is added together with the measurement information, in case, where all available instruments are used, the posterior precision that needs to be inverted in (6) still only has 0.034% nonzero elements.

Next, a simulation study is carried out, where the performance of the method is demonstrated with a known ionosphere taken from the IRI-2012 model. After simulation, the tomography is performed for the real measurements.

A. Simulation

The IRI-2012 model [28] electron densities are shown in Fig. 4, and the altitude integrated electron densities in Fig. 5. The IRI-2012 model was used with its default parameter values.[5] The previously described electron density measurements are simulated with coordinates corresponding to real measurements. The measurement errors are simulated according to the estimated and assumed error distributions given earlier.

The tomographic inversion is then performed several times by adding the measurement sets one by one. The results are shown in Figs. 6–12.

In Fig. 6, only the LEO satellite measurements are used with a zero prior mean profile $\mathbf{x}_{\text{pr}} = \mathbf{0}$. The reconstructed electron density differs from zero only in the vicinity of the areas where the LEO beacon measurements are made. Even in the area of measurements, the electron density is underestimated.

In Fig. 7, again only the LEO satellite measurements are used, but the prior mean for electron densities $\mathbf{x}_{\text{pr}}$ are taken from the simulated ionosonde profile corresponding to the location of EISCAT Dynasonde. The prior mean profile is used as such for the whole domain. Areas far from the measurements remain unchanged from the given prior value.

[5]https://omniweb.gsfc.nasa.gov/vitmo/iri2012_vitmo.html

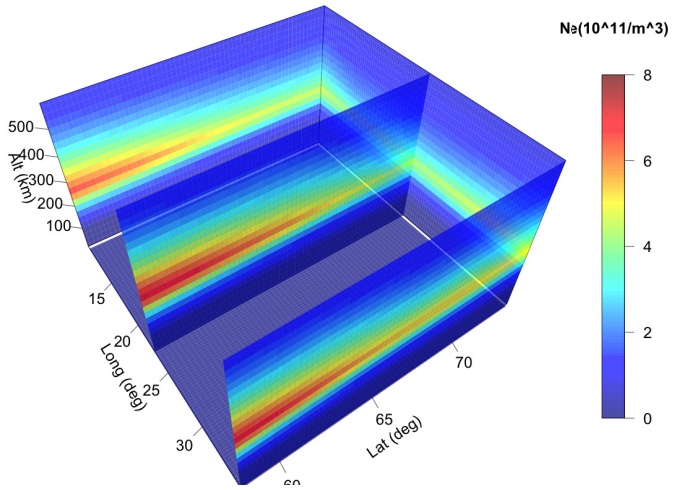

Fig. 8. Simulation case: reconstruction from simulated ground-based LEO and GPS satellite measurements. Simulated ionosonde measurements are used in the scaling of GMRF prior mean and variance mask.

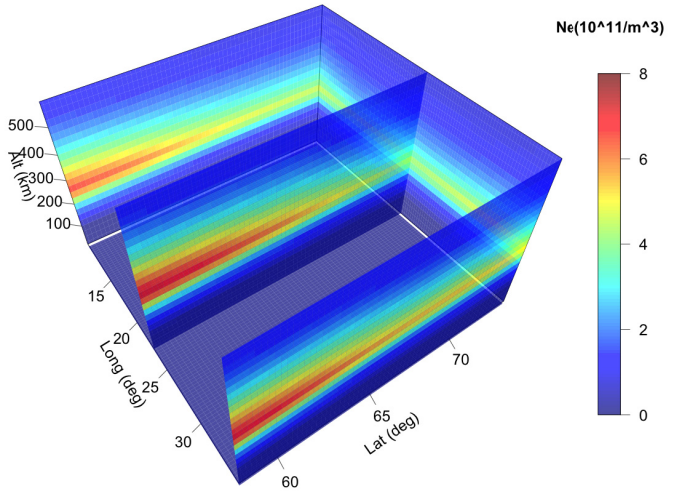

Fig. 9. Simulation case: reconstruction from simulations of ground-based LEO and GPS satellite measurements, ionosonde, satellite *in situ*, and satellite occultation measurements. Simulated ionosonde measurements are used in the scaling of GMRF prior mean and variance mask.

In Fig. 8, the simulated GPS measurements are added to the inversion. The reconstructed electron densities are changed from prior in a much wider area. However, due to the low inclination of GPS satellites, at the higher latitudes, the solution is somewhat dictated by the prior, especially in Northwest corner of the domain.

In Fig. 9, all simulated measurements are added to the inversion. When the ground-based GPS satellite observations are already included, the effect of satellite occultation and *in situ* measurements is mostly invisible. In Fig. 10, the reconstructed electron density is integrated along the altitude similar to Fig. 5. The relative differences between the vertically integrated TEC of IRI-2012 and the last reconstruction with all simulated measurements are shown in Fig. 11.

To demonstrate another aspect of Bayesian approach, the prior and posterior variances, $\boldsymbol{\sigma}^2_{\text{pr}} = \text{diag}(\boldsymbol{\Sigma}_{\text{pr}})$ and

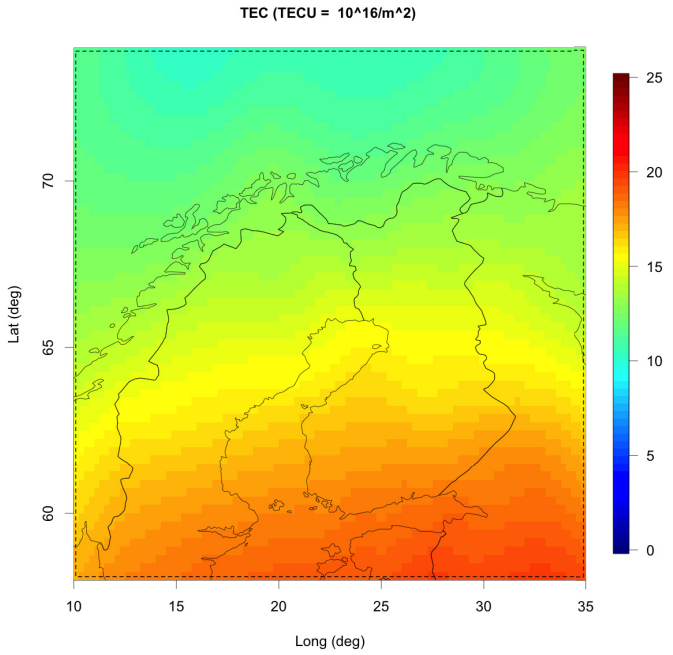

Fig. 10. Simulation case: vertically integrated TEC (0–1250 km) from tomographic reconstruction in Fig. 9.

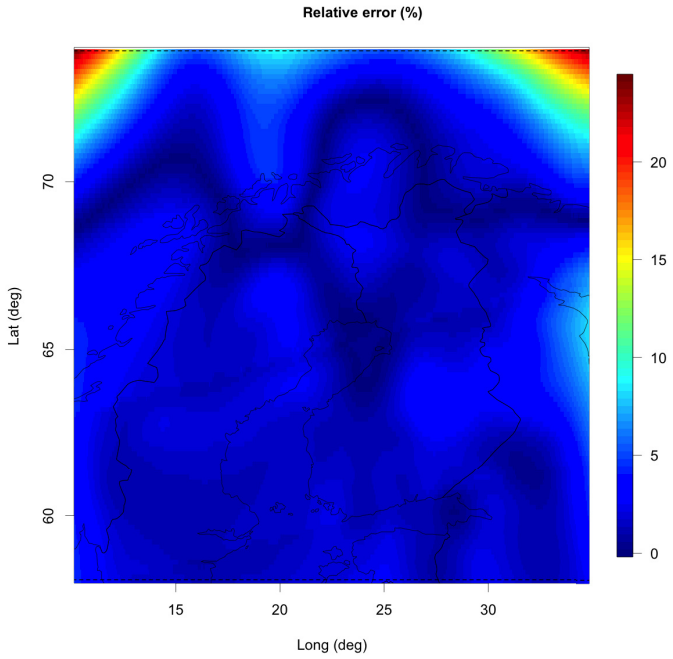

Fig. 11. Simulation case: relative error in vertically integrated TEC (0–1250 km) between IRI-2012 model in Fig. 5 and the tomographic reconstruction in Fig. 9.

$\boldsymbol{\sigma}^2_{\text{post}} = \text{diag}(\boldsymbol{\Sigma}_{\text{post}})$, respectively, are computed to derive $\boldsymbol{\sigma}^2_{\text{expl}} = (1 - (\boldsymbol{\sigma}^2_{\text{post}})/(\boldsymbol{\sigma}^2_{\text{pr}})) \times 100\%$ to describe how much of the prior variance is explained with the measurements. If $\boldsymbol{\sigma}^2_{\text{pr}}$ is not affected by the measurements at all, $\boldsymbol{\sigma}^2_{\text{expl}}$ will be zero and if the information of the measurements is high, $\boldsymbol{\sigma}^2_{\text{expl}}$ will be close to hundred.

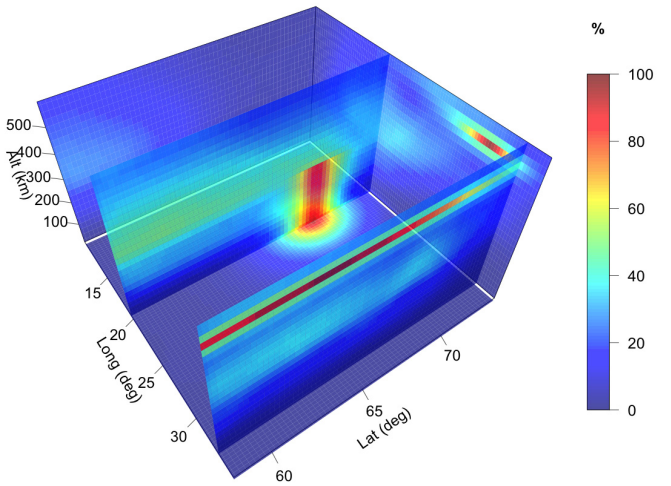

Fig. 12. Explained variance σ^2_{expl} presents the relative difference of prior and posterior variances. When $\sigma^2_{\text{expl}} = 0\%$, the prior assumption is not improved by the measurements at all. When $\sigma^2_{\text{expl}} = 100\%$, the prior uncertainty is explained completely by the measurements. The explained variance depends only on measurement geometry, error and prior covariance. Here, the planes are shifted to longitudes intersecting the ionosonde and Swarm overflight locations.

In Fig. 12, σ^2_{expl} is given for the case where all measurements are included in the computation of σ^2_{post}. As σ^2_{expl} can be visualized in the original grid for the electron density parameters, the uncertainty of the solution can be assessed at different locations. At areas with best measurement coverage, σ^2_{expl} is high. The planes in Fig. 12 are moved to intersect the longitudes of EISCAT Dynasonde and Swarm *in situ* measurements to demonstrate the superior accuracy of the direct measurements. Fig. 12 shows that the satellite *in situ* measurements add information to system, but in this case, the measurements are in such a good agreement that the actual reconstruction is almost unchanged between Figs. 8 and 9.

B. Real Data

The actual GPS measurements are first presented with a single-layer model [17] in Fig. 13, where slant TEC measurements are mapped to vertical TEC, projected to location of 350 km ionospheric pierce points and bilinearly interpolated. The actual pierce points are also shown. Fig. 13 indicates lower TEC compared to IRI model from the same time in Fig. 5; hence, a lower scale is selected to the following visualizations of real data analysis.

In the inversion with real measurements the prior parameter values are unchanged, except for the mean and variance parameters that are scaled according to ionosonde. The 3-D electron density reconstruction is presented in Fig. 14, and the corresponding vertically integrated TEC in Fig. 15. The EISCAT UHF radar beam is projected in Fig. 15, and both ISR profiles are shown in Fig. 16. On top of the measured ISR electron densities are the corresponding profiles from the tomographic reconstruction.

VI. Discussion

The EISCAT ISR validation presented in Fig. 16 is somewhat compromised with the proximity of EISCAT Dynasonde and ISR. Within the model resolution, the VHF radar and Dynasonde are measuring from the very same location. However, as can be seen from Fig. 15, with the low-elevation UHF profile, the location of the measured F-region maximum is several hundred kilometers Southeast from the EISCAT base. In comparison of vertical TEC mapped from GPS measurements in Fig. 13 and TEC integrated from reconstruction in Fig. 15, there is also an agreement between the main features.

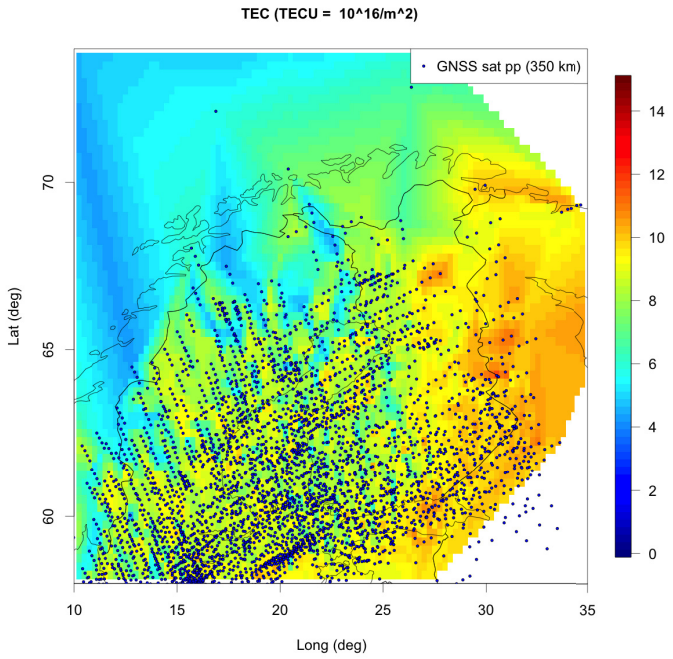

Fig. 13. Real data case: GPS measurements on November 8, 2015 from 10:18:00 UTC to 10:38:00 UTC mapped to vertical TEC with the single-layer model and bilinear interpolation.

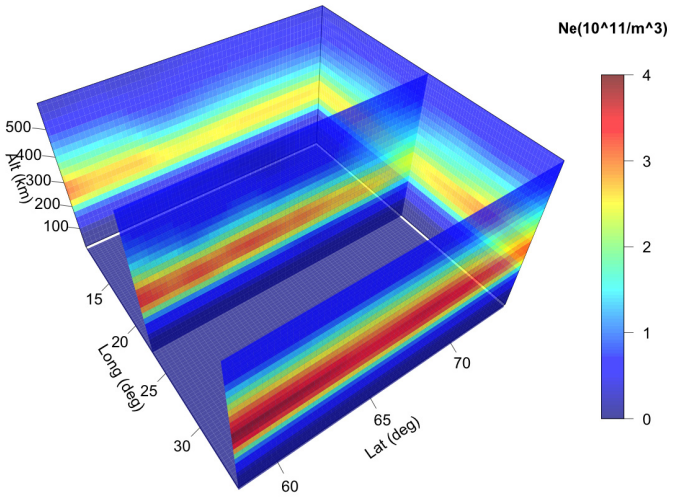

Fig. 14. Real data case: tomographic reconstruction on November 8, 2015 from 10:18:00 UTC to 10:38:00 UTC. Data consist of ground-based LEO and GPS satellite measurements, ionosonde, satellite *in situ*, and satellite occultation measurements. Ionosonde measurements are used in the scaling of GMRF prior mean and variance mask.

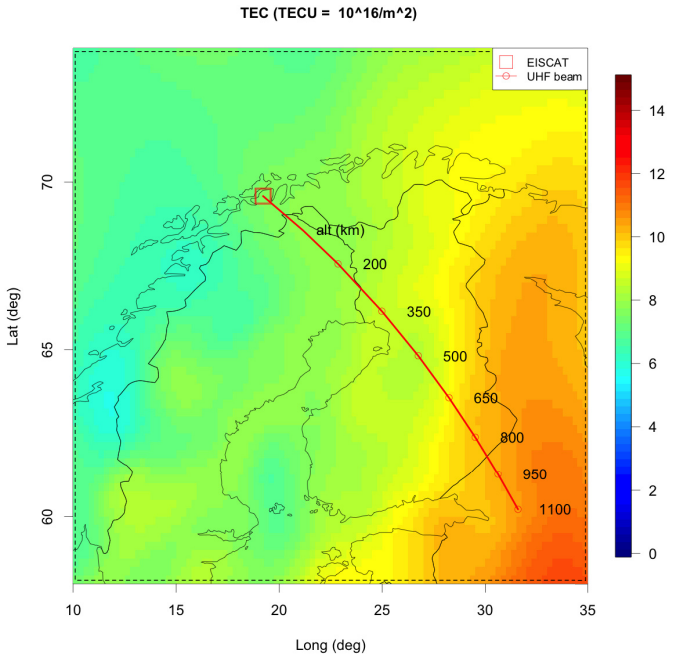

Fig. 15. Real data case: vertically integrated TEC (0–1250 km) from tomographic reconstruction in Fig. 14 with projected EISCAT UHF ISR beam that is used for validation.

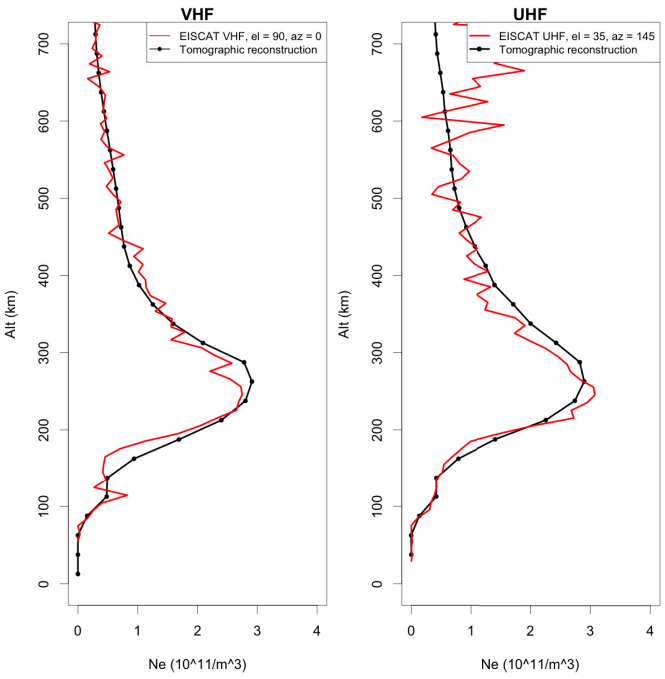

Fig. 16. Real data case: comparison between EISCAT ISR profiles and corresponding profiles from the tomographic reconstruction.

Obviously, for an individual case the parameters could be tuned endlessly; hence, more precise analysis on these results would not give a realistic concept on the overall performance from case to case. In the presented results, the prior parameters were not tuned between the cases, except for the different ionosonde profiles and the first trial with a zero prior. This suggests consistency of the model, but on the other hand, the robustness with respect to changes in the prior parameters was not demonstrated. However, based on the development and work with the model, it can be said that in general, when a realistic prior is chosen, the changes in different parameters produce anticipated changes in the results. Some particular parameters are further discussed in the following.

In comparison of Figs. 13 and 15, the TEC map integrated from the reconstruction might seem slightly over smoothed. This is intuitive as the correlation length parameters were not changed from the simulation case and are relatively long considering the situation in Fig. 13. With shorter correlation lengths, the prior allows more small scale structures in the reconstruction, however, the prior mean dominates more strongly the areas with no measurement, as the effect of the nearby measurements is decreased.

When only LEO RTEC data are used, the distribution of the phase constants γ can have a significant effect. If the phase constant can be approximated beforehand, it improves the accuracy of the absolute level of the solution. When GNSS absolute TEC measurements and direct measurements are in use, the absolute level of LEO TEC can be estimated more accurately within the tomographic inversion.

The GPS measurements used here were already bias corrected. Therefore, a relatively small prior SD could be given for the GPS biases. A trial run was carried out also without the GPS receiver bias correction. The resulting reconstructions with larger bias SD were practically unchanged and the solved biases were very close to preprocessed ones. However, as the model was originally calibrated with bias-corrected data, the performance might be exaggerated with this respect. Then again, it is fair to assume that GNSS biases could be solved to some degree within the inversion, but it would add to general uncertainty of the solutions.

One of the last additions in the presented model was the modeling error. The satellite phase measurements are very accurate and can detect details much finer than a discrete model of this scale can represent. Also, in the time scale of tens of minutes, the changes in ionosphere can be significant. It is then intuitive to relax the model for these factors. In the presented case, the same model without any added modeling error will overestimate the electron density parameters to include unrealistic details.

Here, the nonzero prior mean was extrapolated from the ionosonde measurements horizontally uniformly for the whole domain. This is a rather simple approach and more detailed prior information could also be included. Similar to [14], it is possible to use other sources as the prior mean, for example, ionospheric models such as IRI. However, in regional scale, the models can be significantly off, hence, even a simple model that is based on direct ionospheric measurements is often preferable.

In [14], three methods for taking into account the time propagation were discussed. The presented GMRF prior can be used directly in the two first, where updates are not used at all, or only the background, i.e., the previous MAP-estimate is used without updating the covariance. In addition, instead of full covariance matrix its diagonal, the posterior variance, can be solved and used for scaling of the prediction covariance. Once implemented, the formation of the GMRF precision

matrix is so fast, that if the parameters of covariance function, e.g., the covariance lengths, can be estimated meaningfully, the change of covariance from one time to another does not increase the computation time in practice. For the general case of time propagation, the solution of posterior covariance is a major computational issue. The prediction step is additive for covariance, and the posterior covariance is needed for each time step. Even with the GMRFs, the solution for posterior covariance results a dense matrix and the parametric form is not known. Hence, in the general case, the GMRF contributes only to the first time step, and if the full posterior covariance is required for the subsequent time steps, the sparseness is lost.

VII. Conclusion

It is well known that ionospheric tomography is a very ill-posed problem and the atmospheric electron density cannot be reconstructed without including additional information into the system. It is mostly this information that separates the different tomographic approaches from another. Therefore, it is important to understand the nature of the constraining information in use.

In this paper, first the Bayesian statistical approach for multi-instrument ionospheric tomography is demonstrated. When Gaussian likelihood and prior distributions are assumed, the Bayesian method corresponds computationally to the widely used 3DVAR method. The method provides a clear physical interpretation for the required prior/background information. However, the problem with n unknowns is that it requires representation and operations of an $n \times n$ covariance matrix, and thus becomes computationally complex with large n.

Here, the approach is expanded with the use of GMRF priors to make the problem computationally feasible. In the presented example, a Gaussian prior field with a squared exponential covariance function is approximated with a GMRF. The resulting GMRF has a sparse prior precision matrix with only $25 \times n$ nonzero elements. In comparison to operating with $n \times n$ covariance matrix, this results in a significant decrease in the computational memory and time consumption. In the presented numerical example, the sparse matrix approximation for the $309\,648^2$ posterior precision matrix has only 0.034% nonzero elements, making the computation possible with a modern PC.

It is here shown how the GMRF model is constructed with physically interpretable covariance structure, parameterized with correlation lengths and variance mask, without forming the actual covariance matrix. The performance is validated with results from simulated and real multi-instrument data with comparisons to EISCAT ISR and vertical TEC mapped from original data.

The operative performance depends on how the prior parameters can be fixed or selected dynamically to different ionospheric conditions. Based on the presented results, it is reasonable to expect that this can be done at the level of any present ionospheric tomography system. Further validation of parameter selection requires its own study, which should be performed for consecutive reconstructions for longer time intervals.

VIII. Future Work

The authors are currently working on a 4-D Bayesian filtering for ionospheric tomography, where 3-D reconstructions are made dynamically to consecutive time instants.

Acknowledgment

The GPS data used in this paper are provided by Geotrim (Finland), Swepos (Sweden), and International GNSS service. The GPS data are preprocessed and bias corrected by Massachusetts Institute of Technology Haystack Observatory. The authors are grateful for all the GPS data providers. The authors would like to thank EISCAT scientific association for the ISR and Dynasonde data [EISCAT is an international association supported by research organizations in China (CRIRP), Finland (SA), Japan (NIPR and STEL), Norway (NFR), Sweden (VR), and the United Kingdom (NERC)]. They would also like to thank the International Reference Ionosphere working group for providing the model and data used in this paper, as well as ESA for the Swarm data products.

The authors are grateful for the developers of Multifrontal Massively Parallel sparse direct Solver (MUMPS) that was used in this paper for the computations with an R language interface RMUMPS (https://github.com/morispaa/rmumps).

References

[1] J. R. Austen, S. J. Franke, and C. H. Liu, "Ionospheric imaging using computerized tomography," *Radio Sci.*, vol. 23, no. 3, pp. 299–307, May/Jun. 1988.

[2] V. E. Kunitsyn, E. S. Andreeva, S. J. Franke, and K. C. Yeh, "Tomographic investigations of temporal variations of the ionospheric electron density and the implied fluxes," *Geophys. Res. Lett.*, vol. 30, no. 16, p. 1851, 2003, doi: 10.1029/2003GL016908.

[3] G. S. Bust and C. N. Mitchell, "History, current state, and future directions of ionospheric imaging," *Rev. Geophys.*, vol. 46, no. 1, pp. 1–23, Mar. 2008.

[4] G. K. Seemala, M. Yamamoto, A. Saito, and C.-H. Chen, "Three-dimensional GPS ionospheric tomography over Japan using constrained least squares," *J. Geophys. Res., Space Phys.*, vol. 119, no. 4, pp. 3044–3052, Apr. 2014, doi: 10.1002/2013JA019582.

[5] Y. Yao, J. Tang, P. Chen, S. Zhang, and J. Chen, "An improved iterative algorithm for 3-D ionospheric tomography reconstruction," *IEEE Trans. Geosci. Remote Sens.*, vol. 52, no. 8, pp. 4696–4706, Aug. 2014.

[6] C. H. Chen, A. Saito, C. H. Lin, M. Yamamoto, S. Suzuki, and G. K. Seemala, "Medium-scale traveling ionospheric disturbances by three-dimensional ionospheric GPS tomography 3. Space science," *Earth, Planets Space*, vol. 68, no. 1, pp. 1–9, 2016.

[7] S. Saito, S. Suzuki, M. Yamamoto, A. Saito, and C.-H. Chen, "Real-time ionosphere monitoring by three-dimensional tomography over Japan," *Navigat., J. Inst. Navigat.*, vol. 64, no. 4, pp. 495–504, 2017.

[8] A. Tarantola, *Inverse Problem Theory: Methods for Data Fitting and Model Parameter Estimation*. Amsterdam, The Netherlands: Elsevier, 1987.

[9] J. Kaipio and E. Somersalo, *Statistical and Computational Inverse Problems* (Applied Mathematical Sciences). New York, NY, USA: Springer, 2005.

[10] M. Markkanen *et al.*, "Bayesian approach to satellite radiotomography with applications in the Scandinavian sector," *Ann. Geophys.*, vol. 13, pp. 1277–1287, 1995.

[11] O. Arikan, F. Arikan, and C. B. Erol, "3-D computerized ionospheric tomography with random field priors," in *Mathematical Methods in Engineering*. Dordrecht, The Netherlands: Springer, 2007, pp. 325–334.

[12] J. Norberg, L. Roininen, J. Vierinen, O. Amm, D. McKay-Bukowski, and M. S. Lehtinen, "Ionospheric tomography in Bayesian framework with Gaussian Markov random field priors," *Radio Sci.*, vol. 50, no. 2, pp. 138–152, Feb. 2015.

[13] J. Norberg *et al.*, "Bayesian statistical ionospheric tomography improved by incorporating ionosonde measurements," *Atmos. Meas. Techn.*, vol. 9, no. 4, pp. 1859–1869, 2016.

[14] G. S. Bust, T. W. Garner, and T. L. Gaussiran, II, "Ionospheric Data Assimilation Three-Dimensional (IDA3D): A global, multisensor, electron density specification algorithm," *J. Geophys. Res.*, vol. 109, no. A11, pp. 1–14, 2004.
[15] H. Rue and L. Held, *Gaussian Markov Random Fields: Theory and Applications* (Monographs on Statistics and Applied Probability). Boca Raton, FL, USA: Chapman & Hall, 2005.
[16] J. Vierinen *et al.*, "Beacon satellite receiver for ionospheric tomography," *Radio Sci.*, vol. 49, no. 12, pp. 1141–1152, 2014.
[17] I. Horvath and S. Crozier, "Software developed for obtaining GPS-derived total electron content values," *Radio Sci.*, vol. 42, no. 2, pp. 1–20, 2007.
[18] W. Rideout and A. Coster, "Automated GPS processing for global total electron content data," *GPS Solutions*, vol. 10, no. 3, pp. 219–228, 2006. [Online]. Available: https://link.springer.com/content/pdf/10.1007%2Fs10291-006-0029-5.pdf
[19] J. Vierinen, A. J. Coster, W. C. Rideout, P. J. Erickson, and J. Norberg, "Statistical framework for estimating GNSS bias," *Atmos. Meas. Techn.*, vol. 9, no. 3, pp. 1303–1312, 2016.
[20] R. Furrer, M. G. Genton, and D. Nychka, "Covariance tapering for interpolation of large spatial datasets," *J. Comput. Graph. Statist.*, vol. 15, no. 3, pp. 502–523, 2006.
[21] L. Roininen, M. S. Lehtinen, S. Lasanen, M. Orispää, and M. Markkanen, "Correlation priors," *Inverse Problems Imag.*, vol. 5, no. 1, pp. 167–184, 2011.
[22] L. Roininen, P. Piiroinen, and M. Lehtinen, "Constructing continuous stationary covariances as limits of the second-order stochastic difference equations," *Inverse Problems Imag.*, vol. 7, no. 2, pp. 611–647, 2013.
[23] F. Lindgren, H. Rue, and J. Lindström, "An explicit link between Gaussian fields and Gaussian Markov random fields: The stochastic partial differential equation approach," *J. Roy. Statist. Soc. Ser. B*, vol. 73, no. 4, pp. 423–498, 2011, doi: 10.1111/j.1467-9868.2011.00777.x.
[24] L. Roininen, S. Lasanen, M. Orispää, and S. Särkkä, "Sparse approximations of fractional Matérn fields," *Scandin. J. Statist.*, vol. 45, no. 1, pp. 194–216, 2018.
[25] T. N. Davis and M. Sugiura, "Auroral electrojet activity index AE and its universal time variations," *J. Geophys. Res.*, vol. 71, no. 3, pp. 785–801, Feb. 1966, doi: 10.1029/JZ071i003p00785.
[26] N. Olsen *et al.*, "The *Swarm* Satellite Constellation Application and Research Facility (SCARF) and Swarm data products," *Earth, Planets Space*, vol. 65, no. 11, p. 1, Nov. 2013, doi: 10.5047/eps.2013.07.001.
[27] N. A. Zabotin, J. W. Wright, and G. A. Zhbankov, "NeXtYZ: Three-dimensional electron density inversion for dynasonde ionograms," *Radio Sci.*, vol. 41, no. 6, pp. 1–12, Dec. 2006, doi: 10.1029/2005RS003352.
[28] D. Bilitza *et al.*, "The International Reference Ionosphere 2012—A model of international collaboration," *J. Space Weather Space Climate*, vol. 4, p. A07, Feb. 2014. [Online]. Available: https://www.swsc-journal.org/articles/swsc/pdf/2014/01/swsc130043.pdf, doi: 10.1051/swsc/2014004.
[29] J. M. Dow, R. Neilan, and C. Rizos, "The international GNSS service in a changing landscape of global navigation satellite systems," *J. Geodesy*, vol. 83, nos. 3–4, pp. 191–198, Mar. 2009. [Online]. Available: https://link.springer.com/content/pdf/10.1007%2Fs00190-008-0300-3.pdf
[30] P. R. Amestoy, I. S. Duff, J.-Y. L'Excellent, and J. Koster, "A fully asynchronous multifrontal solver using distributed dynamic scheduling," *SIAM J. Matrix Anal. Appl.*, vol. 23, no. 1, pp. 15–41, 2001, doi: doi/pdf/10.1137/S0895479899358194.
[31] P. R. Amestoy, A. Guermouche, J.-Y. L'Excellent, and S. Pralet, "Hybrid scheduling for the parallel solution of linear systems," *Parallel Comput.*, vol. 32, no. 2, pp. 136–156, Feb. 2006. [Online]. Available: http://linkinghub.elsevier.com/retrieve/pii/S0167819105001328

Johannes Norberg received the Ph.D. degree in applied mathematics from the University of Helsinki, Helsinki, Finland.

He is currently a Research Scientist with the Finnish Meteorological Institute, Helsinki. He is involved in inverse problems and scientific computing. He is responsible for the TomoScand Project for instrumentation and algorithm development for ionospheric tomography.

Juha Vierinen received the M.S. and Ph.D. degrees from the Helsinki University of Technology, Espoo, Finland, in 2005 and 2012, respectively.

From 2013 to 2016, he was with Massachusetts Institute of Technology Haystack Observatory, Westford, MA, USA. He is currently an Associate Professor of space physics with the University of Tromsø, Tromsø, Norway. His research interests include the development of novel radar and radio remote sensing measurement techniques to study space plasmas.

Lassi Roininen is currently an Adjunct Professor of applied mathematics with the University of Oulu, Oulu, Finland, and also a Post-Doctoral Researcher with the Academy of Finland, Sodankylä Geophysical Observatory, University of Oulu. He is involved in rigorous numerical and computational tools for inverse problems with applications in near-space remote sensing, subsurface imaging, and X-ray tomography.

Mikko Orispää received the Ph.D. degree in mathematics from the University of Oulu, Oulu, Finland, in 2002.

He is involved in inverse problems and scientific computing. He is currently an Application Designer with Sodankylä Geophysical Observatory, University of Oulu, where his responsibilities include the research and development of new measurement methods, and the development of scientific software for the measurement device operation, measurement data handling, and analysis.

Kirsti Kauristie was a Coordinator in several research projects funded by ESA and EU. She has co-authored 95 refereed articles (h-index 17). Her research interests include high-latitude ionospheric physics: Auroras, their electrodynamics, and variations in the ionospheric electron content.

Ms. Kauristie has been representing Finland in the Program Board of the ESA Space Situational Awareness Program since 2012. Since 2017, she has been a member of the Space Weather Assessment and Consolidation Working Group established by the European Science Foundation. She has served as a Topical Editor for the EGU Journal Annales Geophysicae from 2008 to 2012, the Council Chair for the EISCAT Association from 2009 to 2010, and the Co-Chair for the Team which composed the Cospar/ILWS Roadmap for Space Weather Research from 2015 to 2025.

William C. Rideout was born in East Orange, NJ, USA, in 1958. He received the B.A. degree in physics and English literature from Bucknell University, Lewisburg, PA, USA, in 1980, the master's degree from the Massachusetts Institute of Technology, Cambridge, MA, USA, in 1985, and the master's degree in computer engineering from the University of Massachusetts, Lowell, MA, USA, in 2001.

Since 2001, he has been with Massachusetts Institute of Technology Haystack Observatory, Westford, MA, USA.

Anthea J. Coster received the Ph.D. degree from Rice University, Houston, TX, USA, in 1983.

She was with Arecibo Observatory, Arecibo, Puerto Rico. She has been involved with GPS since 1985, and leads the Global Navigation Satellite System (GNSS) Research Program at Haystack. She is currently an Assistant Director and a Principal Research Scientist with Massachusetts Institute of Technology Haystack Observatory, Westford, MA, USA. Her research interests include space weather, ionospheric and atmospheric coupling, and GNSS positioning and measurement accuracy.

Markku S. Lehtinen is currently a Research Professor with Sodankylä Geophysical Observatory, University of Oulu, Oulu, Finland. He is currently an internationally recognized leading expert in statistical inverse methods and applications in incoherent scatter radar studies. He has developed measurement principles, as well as radar construction principles for the next-generation incoherent scatter radar EISCAT_3D.